

A Third-Order Moving Mesh Cell-Centered Scheme for One-Dimensional Elastic-Plastic Flows

Jun-Bo Cheng^{*} Weizhang Huang[†] Song Jiang[‡] Baolin Tian[§]

A third-order moving mesh cell-centered scheme without the remapping of physical variables is developed for the numerical solution of one-dimensional elastic-plastic flows with the Mie-Grüneisen equation of state, the Wilkins constitutive model, and the von Mises yielding criterion. The scheme combines the Lagrangian method with the MMPDE moving mesh method and adaptively moves the mesh to better resolve shock and other types of waves while preventing the mesh from crossing and tangling. It can be viewed as a direct arbitrarily Lagrangian-Eulerian method but can also be degenerated to a purely Lagrangian scheme. It treats the relative velocity of the fluid with respect to the mesh as constant in time between time steps, which allows high-order approximation of free boundaries. A time dependent scaling is used in the monitor function to avoid possible sudden movement of the mesh points due to the creation or diminishing of shock and rarefaction waves or the steepening of those waves. A two-rarefaction Riemann solver with elastic waves is employed to compute the Godunov values of the density, pressure, velocity, and deviatoric stress at cell interfaces. Numerical results are presented for three examples. The third-order convergence of the scheme and its ability to concentrate mesh points around shock and elastic rarefaction waves are demonstrated. The obtained numerical results are in good agreement with those in literature. The new scheme is also shown to be more accurate in resolving shock and rarefaction waves than an existing third-order cell-centered Lagrangian scheme.

Key Words. Elastic-plastic flows; Cell-centered Lagrangian scheme; Moving mesh method; High order scheme; Hypoelastic constitutive model

Abbreviated title. A third-order moving mesh scheme for elastic-plastic flows

^{*}Laboratory of Computational Physics, Institute of Applied Physics and Computational Mathematics, Beijing, China
(*cheng_junbo@iapcm.ac.cn*)

[†]Department of Mathematics, the University of Kansas, Lawrence, KS 66045, U.S.A. (*whuang@ku.edu*)

[‡]Laboratory of Computational Physics, Institute of Applied Physics and Computational Mathematics, Beijing, China
(*jiang@iapcm.ac.cn*)

[§]Laboratory of Computational Physics, Institute of Applied Physics and Computational Mathematics, Beijing, China
(*tian_baolin@iapcm.ac.cn*)

1 Introduction

We consider the numerical simulation of one-dimensional (1D) elastic-plastic solid problems with the isotropic elastic-plastic model initially developed by Wilkins [35] where a perfectly elastic material is characterized by Hooke's law in the sense that an incremental strain results in an incremental stress and the elastic limit is described by the von Mises yielding criterion.

Numerical methods for elastic-plastic flows can be roughly classified into three categories. The first is staggered Lagrangian schemes, first developed by Wilkins [35], which discretize the equations of momentum and specific internal energy on a staggered mesh and use artificial viscosity to suppress spurious numerical oscillations around shock waves. The second is Eulerian methods, e.g., see [4, 12, 26, 28, 34], which are often used for hyperelastic models that can be formulated in the conservative form. The third, which is considered in this work, is cell-centered Lagrangian schemes that have recently attracted considerable attention from researchers (e.g., see [9, 10, 11, 22, 25, 31]). They are conservative and can resolve shock waves without using artificial viscosity and be used for both hyperelastic and hypoelastic models. However, the major disadvantage of these schemes is that the mesh, which moves at the flow velocity, can easily cross over or become tangling.

Arbitrary Lagrangian-Eulerian (ALE) methods, first introduced by Hirt, Amsden, and Cook [13], have been designed to overcome this disadvantage. Usually, ALE methods contain three phases, the pure Lagrangian phase, a rezone phase, and a remapping phase. Different from general ALE methods, direct ALE methods have been implemented directly without the need for interpolation (i.e. remapping) of physical variables between different meshes. For example, Luo et al. [24] introduce second-order direct ALE HLLCE and Godunov schemes to solve the problems of multi-material flows while high-order direct ALE finite volume and discontinuous Galerkin (DG) schemes are proposed in [5, 6] and [29, 30], respectively. Unlike their traditional counterparts, which can readily handle free boundary domains in the Lagrangian phase and allow the mesh to move arbitrarily in the rezone phase, these direct ALE methods are not considered to deal with free boundary problems where the boundary moves at the flow velocity (which is part of the solutions to be sought) and therefore cannot be purely Lagrangian [6, 29]. Direct ALE methods have been successfully applied to hyperelastic-plastic flows in [6].

Interestingly, ALE methods form a special type of moving mesh methods. In the past, a number of other moving mesh methods have been developed; e.g., see [2, 8, 18, 19, 23, 27]. The interested reader is also referred to the books/review articles [1, 3, 7, 20, 32] and references therein. In this work, we consider combining an cell-centered Lagrangian scheme with an error-based moving mesh method which is known to be more robust in preventing the mesh from crossing and tangling. We will use the so-called MMPDE (moving mesh partial differential equation) moving mesh method [17, 18, 20] which is capable of concentrating mesh points according to a user-supplied monitor function and preventing the mesh from becoming singular in one and multiple dimensions [16]. It also has the advantages of being relatively simple, compact, and easy to implement and working for both convex and concave domains [15]. By combining the Lagrangian and MMPDE methods, we hope that the new method will inherit the advantages of both methods. Moreover, although we focus on 1D problems in the current work, we hope that the new method can be used for multi-dimensional problems.

More specifically, we will develop a third-order moving mesh cell-centered scheme (MMCC) for 1D elastic-plastic flows. The scheme can be viewed as a new direct ALE method. Indeed, like the existing

direct ALE methods [5, 6, 24, 29, 30], MMCC scheme does not need the remapping of physical variables between different meshes. But it also possesses a unique feature that other direct ALE methods do not have, that is, it can be degenerated to a purely Lagrangian scheme. This is done by introducing the relative velocity of the fluid with respect to the moving mesh as a new variable w . When $w = 0$, the MMCC scheme reduces to a purely Lagrangian scheme (CCL) proposed by Cheng et al. [11]. Moreover, the introduction of w makes it relatively easy to simulate free boundary problems for which we can simply set $w = 0$ on the boundary (so the boundary nodes move at the Lagrangian velocity). Furthermore, the mesh velocity is commonly treated in existing moving mesh methods as constant in time between time steps, which typically results in low-order approximation of free boundaries (e.g, see [14]). MMCC treats w as constant in time instead, and this new treatment allows high-order approximation of free boundaries. In fact, like CCL, MMCC is also third-order accurate (and conservative and essentially non-oscillatory). In addition, it has the ability to concentrate mesh points around shock waves and elastic rarefaction waves.

An outline of the paper is as follows. The governing equations of elastic-plastic flows are described in Section 2. The MMCC scheme is presented in Section 3, followed by numerical examples in Section 4. The conclusions are drawn in Section 5.

2 Governing equations

The 1D governing equations of the isotropic elastic-plastic model of [35] for elastic-plastic flows read as

$$\frac{\partial}{\partial t} \mathbf{U} + \frac{\partial}{\partial x} \mathbf{F}(\mathbf{U}) = 0, \quad x \in \Omega, \quad t > 0 \quad (1)$$

where Ω is an interval,

$$U = \begin{bmatrix} \rho \\ \rho u \\ \rho E \end{bmatrix}, \quad F = \begin{bmatrix} \rho u \\ \rho u^2 - \sigma_x \\ (\rho E - \sigma_x) u \end{bmatrix}, \quad (2)$$

ρ is the density, u is the velocity in the x -direction, $E = e + \frac{1}{2}u^2$ is the total energy density, e is the specific internal energy, and σ_x is the Cauchy stress which is related to the hydrostatic pressure (p) and the deviatoric stress (s_{xx}) as

$$\sigma_x = -p + s_{xx}. \quad (3)$$

Following the convention in mechanics, we use σ_x and s_{xx} here to denote the components of the corresponding variables in x direction; this is different from the mathematical convention where subscription x typically denotes the differentiation with respect to x . The pressure is related to the internal energy and the density through the equation of state (EOS). In this work we use the Mie-Grüneisen EOS,

$$p(\rho, e) = \rho_0 a_0^2 \frac{(\eta - 1) [\eta - \Gamma_0(\eta - 1)/2]}{[\eta - s(\eta - 1)]^2} + \rho_0 \Gamma_0 e, \quad (4)$$

where $\eta = \rho/\rho_0$ and ρ_0 , a_0 , s , and Γ_0 are constant parameters. The elastic energy is not included in the above model as it is negligible in many practical engineering problems (e.g., see [25]).

The relation between the deviatoric stress and the strain is described by Hooke's law. It reads as

$$\dot{s}_{xx} = 2\mu \left(\dot{\epsilon}_x - \frac{1}{3} \dot{V} \right), \quad (5)$$

where μ is the shear modulus, V is volume, the dot denotes the material time derivative, and

$$\dot{\epsilon}_x = \frac{\partial u}{\partial x}, \quad \frac{\dot{V}}{V} = \frac{\partial u}{\partial x}.$$

Combining the above equations we get

$$\frac{\partial s_{xx}}{\partial t} + u \frac{\partial s_{xx}}{\partial x} = \frac{4\mu}{3} \frac{\partial u}{\partial x}. \quad (6)$$

The von Mises yielding condition is used here to describe the elastic limit. In one dimension, it takes the form

$$|s_{xx}| \leq \frac{2}{3} Y_0, \quad (7)$$

where Y_0 is the yield strength of the material in simple tension. This condition is enforced in the numerical solution of (1) and (6); cf. (26).

For the numerical examples we consider in Section 4, free/fixed boundaries with periodic, Dirichlet, and/or wall boundary conditions are used, depending on the specific setting of each example. Thus, it is important that any scheme designed for (1) and (6) can approximate free boundaries with high-order accuracy.

3 A third-order moving mesh cell-centered scheme

3.1 The overall procedure

With the MMCC method, the governing equations (1) and (6) are discretized on a moving mesh

$$x_{\frac{1}{2}}(t) < x_{\frac{3}{2}}(t) < \cdots < x_{N-\frac{1}{2}}(t) < x_{N+\frac{1}{2}}(t), \quad (8)$$

where N is the number of cells in the mesh. The mesh is moved using a combination of the Lagrangian and MMPDE moving mesh velocities [17, 18, 20]. This is different from most of the existing moving mesh methods (e.g., see [7, 20]) where one of the velocities, but not both, is used. By combining the velocities, we hope that the new method can inherit the advantages of both, especially being able to concentrate mesh points around shock waves and some other places of interest (for instance, the region of large gradient of s_{xx} in our current situation) while preventing the mesh from crossing and tangling.

Another main difference between MMCC and the existing moving mesh methods lies in the numerical treatment of the mesh speed (\dot{x}). It is common practice (e.g., see [20]) that \dot{x} is approximated to be constant in time between time steps. A disadvantage of this is that the trajectories of the boundary points are linear in time, which gives a second-order approximation to free boundaries (that move at the flow velocity in the current situation). To allow higher-order approximations, we propose to treat the relative flow velocity with respect to the mesh, $w = u - \dot{x}$, as constant between time steps instead. With this, we can assure that w be zero and thus $\dot{x} = u$ on the free boundary. Thus, the scheme is purely Lagrangian on the free boundary. Moreover, a high-order approximation to the location of the free boundary can be obtained by integrating $\dot{x} = u$ (see the detail in Section 3.3).

The steps of the MMCC method are given in the following and will be elaborated in the subsequent subsections.

(i) Given the cell average \bar{Q} of $Q = (\rho, \rho u, \rho E, s_{xx})^T$, the Lagrangian velocity $u_{i+\frac{1}{2}}^n$, $i = 0, \dots, N$ is evaluated using the two-rarefaction Riemann solver with elastic wave (TRRSE) [11]. Notice that (6) is not in conservative form. TRRSE is specially designed for the nonconservative system (1) and (6) in primitive variables by assuming that all nonlinear waves are continuous rarefaction waves and solving the equations for the generalized Riemann invariants across rarefactions; see [11] for the detail. Like a two-rarefaction Riemann solver (TRRS) in [33] for pure fluids, TRRSE has proven robust and accurate for elastic-plastic flows [11].

(ii) The Lagrangian coordinate of the mesh points are computed as

$$\hat{x}_{i+\frac{1}{2},L}^{n+1} = x_{i+\frac{1}{2}}^n + u_{i+\frac{1}{2}}^n \Delta t^{n-\frac{1}{2}}, \quad i = 0, \dots, N \quad (9)$$

where $\Delta t^{n-\frac{1}{2}} = t^n - t^{n-1}$.

(iii) (Section 3.2) Based on $\hat{x}_{i+\frac{1}{2},L}^{n+1}$, $i = 0, \dots, N$, the MMPDE method is used to generate a new mesh $\hat{x}_{i+\frac{1}{2}}^{n+1}$, $i = 0, \dots, N$ with boundary conditions $\hat{x}_{\frac{1}{2}}^{n+1} = \hat{x}_{\frac{1}{2},L}^{n+1}$ and $\hat{x}_{N+\frac{1}{2}}^{n+1} = \hat{x}_{N+\frac{1}{2},L}^{n+1}$.

(iv) The relative velocity is computed as

$$w_{i+\frac{1}{2}} = u_{i+\frac{1}{2}}^n - \frac{\hat{x}_{i+\frac{1}{2}}^{n+1} - x_{i+\frac{1}{2}}^n}{\Delta t^{n-\frac{1}{2}}}, \quad i = 0, \dots, N \quad (10)$$

and is treated as constant in time from t_n to t_{n+1} . Notice that $w_{\frac{1}{2}} = w_{N+\frac{1}{2}} = 0$ and thus the boundary mesh nodes move at the flow velocity.

(v) (Section 3.4) The new time step size Δt^n is estimated using the CFL condition. Set $t^{n+1} = t^n + \Delta t^n$.

(vi) (Section 3.3) The third-order Runge-Kutta method and third-order finite volume numerical fluxes are used to compute \bar{Q}_i^{n+1} , $i = 1, \dots, N$, and $x_{i+\frac{1}{2}}^{n+1}$, $i = 0, \dots, N$. The MMCC method is expected to be of third order in both time and space.

3.2 Mesh movement by the MMPDE method

The MMPDE method is a variational method that generates the mesh through a coordinate transformation $x = x(\xi, t) : (0, 1) \rightarrow (a, b)$ (with $a = \hat{x}_{\frac{1}{2},L}^{n+1}$ and $b = \hat{x}_{N+\frac{1}{2},L}^{n+1}$ being fixed for this time step), viz.,

$$x_{i+\frac{1}{2}}(t) = x(\hat{\xi}_{i+\frac{1}{2}}, t), \quad i = 0, \dots, N$$

where $\hat{\xi}_{i+\frac{1}{2}} = i/N$, $i = 0, \dots, N$ is a uniform mesh on $(0, 1)$. The inverse of the coordinate transformation, $\xi = \xi(x, t)$, is governed by an MMPDE defined as the gradient flow equation of a meshing functional. We use the functional

$$I[\xi] = \frac{1}{2} \int_a^b \frac{1}{M} \left(\frac{\partial \xi}{\partial x} \right)^2 dx, \quad (11)$$

where M is the monitor function that is defined to measure difficulty in approximating the physical solution. The Euler-Lagrange equation of the functional is

$$-\frac{\partial}{\partial x} \left(\frac{1}{M} \frac{\partial \xi}{\partial x} \right) = 0,$$

which is mathematically equivalent to the well-known equidistribution principle,

$$M \frac{\partial x}{\partial \xi} = \sigma, \quad \sigma = \int_a^b M dx.$$

Then the MMPDE is defined as

$$\frac{\partial \xi}{\partial t} = \frac{M}{\tau} \frac{\partial}{\partial x} \left(\frac{1}{M} \frac{\partial \xi}{\partial x} \right), \quad (12)$$

where $\tau > 0$ is a parameter used to adjust the response time scale of the mesh movement to the changes in M . The smaller τ is, the more quickly the mesh movement responds to the changes in M . We take $\tau = 0.01$ in our computation.

Recall that our goal is to generate the new mesh $\hat{x}_{i+\frac{1}{2}}^{n+1}$, $i = 0, \dots, N$ from the Lagrangian mesh $\hat{x}_{i+\frac{1}{2},L}^{n+1}$, $i = 0, \dots, N$. To this end, we discretize (12) on the Lagrangian mesh using central finite differences in space and the backward Euler in time. We have

$$\frac{\xi_{i+\frac{1}{2}}^{n+1} - \hat{\xi}_{i+\frac{1}{2}}}{\Delta t} = \frac{M_{i+\frac{1}{2}}}{\tau(\hat{x}_{i+1,L}^{n+1} - \hat{x}_{i,L}^{n+1})} \left[\frac{1}{M_{i+1}} \frac{(\xi_{i+\frac{3}{2}}^{n+1} - \xi_{i+\frac{1}{2}}^{n+1})}{(\hat{x}_{i+\frac{3}{2},L}^{n+1} - \hat{x}_{i+\frac{1}{2},L}^{n+1})} - \frac{1}{M_i} \frac{(\xi_{i+\frac{1}{2}}^{n+1} - \xi_{i-\frac{1}{2}}^{n+1})}{(\hat{x}_{i+\frac{1}{2},L}^{n+1} - \hat{x}_{i-\frac{1}{2},L}^{n+1})} \right], \quad (13)$$

where $M_i = \frac{1}{2}(M_{i+\frac{1}{2}} + M_{i-\frac{1}{2}})$, $\hat{x}_{i,L} = \frac{1}{2}(\hat{x}_{i+\frac{1}{2},L} + \hat{x}_{i-\frac{1}{2},L})$, and the uniform computational mesh has been taken as the initial mesh for the integration. The above equation, together with the boundary conditions,

$$\xi_{\frac{1}{2}}^{n+1} = 0, \quad \xi_{N+\frac{1}{2}}^{n+1} = 1,$$

forms a linear algebraic system that can be solved for the new computational mesh $\xi_{i+\frac{1}{2}}^{n+1}$, $i = 0, \dots, N$. This mesh and the Lagrangian mesh define a correspondence relation, denoted by

$$x = \Phi_h(\xi) \quad \text{or} \quad \hat{x}_{i+\frac{1}{2},L}^n = \Phi_h(\xi_{i+\frac{1}{2}}^{n+1}), \quad i = 0, \dots, N.$$

Then, the new physical mesh is defined as

$$\hat{x}_{i+\frac{1}{2}}^{n+1} = \Phi_h(\hat{\xi}_{i+\frac{1}{2}}), \quad i = 0, \dots, N$$

which can be obtained through linear interpolation.

We now consider the definition of the monitor function. The entropy is commonly used for adaptive mesh simulation of shock waves. However, in the current situation the complexity of the EOS and the presence of the deviatoric stress make it difficult to compute the entropy exactly. For this reason, we use the density and deviatoric stress, which have jumps around shock waves and elastic limits, respectively. First, the derivatives of ρ and s_{xx} are computed,

$$\left(\frac{\partial \rho}{\partial x} \right)_{i+\frac{1}{2}} = \frac{\bar{\rho}_{i+1,L}^{n+1} - \bar{\rho}_{i,L}^{n+1}}{\hat{x}_{i+1,L}^{n+1} - \hat{x}_{i,L}^{n+1}}, \quad \left(\frac{\partial s_{xx}}{\partial x} \right)_{i+\frac{1}{2}} = \frac{(\overline{s_{xx}})_{i+1}^n - (\overline{s_{xx}})_i^n}{x_{i+1}^n - x_i^n},$$

where

$$\bar{\rho}_{i+1,L}^{n+1} = \frac{\bar{\rho}_{i+1}^n \left(x_{i+\frac{1}{2}}^n - x_{i-\frac{1}{2}}^n \right)}{\widehat{x}_{i+\frac{1}{2},L}^{n+1} - \widehat{x}_{i-\frac{1}{2},L}^{n+1}}.$$

Notice that the value of s_{xx} at t_n has been used since it is not constant along a particle trajectory. Having obtained the derivatives, we define

$$\widehat{M}_{i+\frac{1}{2}}^{(n)} = \sqrt{1 + \left(\frac{\partial \rho}{\partial x} \right)_{i+\frac{1}{2}}^2 + \alpha \left(\frac{\partial s_{xx}}{\partial x} \right)_{i+\frac{1}{2}}^2}, \quad (14)$$

where

$$\alpha = \left[\frac{\max_i \left| \left(\frac{\partial \rho}{\partial x} \right)_{i+\frac{1}{2}} \right|}{\max_i \left| \left(\frac{\partial s_{xx}}{\partial x} \right)_{i+\frac{1}{2}} \right|} \right]^2. \quad (15)$$

The scaling factor α is used in the above since the magnitude of the jumps in the density is much larger than those in the deviatoric stress in general. This scaling is necessary for concentrating mesh points around the elastic limit.

Since jumps such as shock waves can disappear or be created, the ratio of the maximum value to the minimum value of the monitor function defined in (14) can change dramatically over time. To avoid these dramatic changes, we further scale the monitor function using the current and past ratios of the maximum and minimum values of the monitor function and define

$$M_{i+\frac{1}{2}} = \widehat{M}_{Min}^{(n)} + \frac{M_{critic} - \widehat{M}_{Min}^{(n)}}{\widehat{M}_{Max}^{(n)} - \widehat{M}_{Min}^{(n)}} \left(\widehat{M}_{i+\frac{1}{2}}^{(n)} - \widehat{M}_{Min}^{(n)} \right), \quad (16)$$

where

$$\begin{aligned} \widehat{M}_{Min}^{(n)} &= \min_i \left(\widehat{M}_{i+\frac{1}{2}}^{(n)} \right), & \widehat{M}_{Max}^{(n)} &= \max_i \left(\widehat{M}_{i+\frac{1}{2}}^{(n)} \right), \\ M_{critic} &= \min \left(10, \max_{k=1, \dots, n} \frac{\widehat{M}_{Max}^{(k)}}{\widehat{M}_{Min}^{(k)}} \right) \widehat{M}_{Min}^{(n)}. \end{aligned}$$

The so-defined monitor function is further smoothed in space in order to produce a mesh that is also smooth in space. We use

$$\frac{1}{4}M_{i+\frac{3}{2}} + \frac{1}{2}M_{i+\frac{1}{2}} + \frac{1}{4}M_{i-\frac{1}{2}} \rightarrow M_{i+\frac{1}{2}}$$

for the interior points and a similar formula for the boundary points. This scheme is applied $N/40$ sweeps every time a new monitor function is computed.

3.3 A third-order cell-centered scheme on moving meshes

We now describe a third-order cell-centered discretization for (1) and (6) under appropriate initial and boundary conditions on the moving mesh (8). Denote $I_i = (x_{i-\frac{1}{2}}, x_{i+\frac{1}{2}})$, $\Delta x_i = x_{i+\frac{1}{2}} - x_{i-\frac{1}{2}}$, and

the center of I_i by x_i . A semi-discrete finite volume discretization of the conservative equation (1) over the cell I_i is given by

$$\frac{d(\overline{\mathbf{U}}_i \Delta x_i)}{dt} = - \left(\mathbf{F}_{i+\frac{1}{2}} - \mathbf{F}_{i-\frac{1}{2}} \right), \quad (17)$$

where $\overline{\mathbf{U}}_i$ is the numerical approximation to the average of U over I_i and $\mathbf{F}_{i+\frac{1}{2}}$ is the numerical flux at the cell boundary $x_{i+\frac{1}{2}}$ (and $\mathbf{F}_{i-\frac{1}{2}}$ is the numerical flux at $x_{i-\frac{1}{2}}$). It is defined as

$$\mathbf{F}_{i+\frac{1}{2}} = F(\mathbf{Q}_{i+\frac{1}{2}}) = \begin{bmatrix} \rho_{i+\frac{1}{2}} w_{i+\frac{1}{2}} \\ p_{i+\frac{1}{2}} - (s_{xx})_{i+\frac{1}{2}} + \rho_{i+\frac{1}{2}} u_{i+\frac{1}{2}} w_{i+\frac{1}{2}} \\ \left(p_{i+\frac{1}{2}} - (s_{xx})_{i+\frac{1}{2}} \right) u_{i+\frac{1}{2}} + \rho_{i+\frac{1}{2}} E_{i+\frac{1}{2}} w_{i+\frac{1}{2}} \end{bmatrix}, \quad (18)$$

where $\mathbf{Q}_{i+\frac{1}{2}}$ denotes the Godunov value of $\mathbf{Q} = (\rho, \rho u, \rho E, s_{xx})^T$ to the Riemann problem with the left and right states, $\mathbf{Q}_{i+\frac{1}{2}}^-$ and $\mathbf{Q}_{i+\frac{1}{2}}^+$ (which are the left and right limits of \mathbf{Q} at $x_{i+\frac{1}{2}}$, respectively). Note that mesh movement has been taken into consideration and \dot{x} has been replaced by $\dot{x} = u - w$. In the following, we explain how to compute $\mathbf{Q}_{i+\frac{1}{2}}$ and $\mathbf{Q}_{i+\frac{1}{2}}^\pm$.

The limits $\mathbf{Q}_{i+\frac{1}{2}}^\pm$ are computed using the third-order WENO reconstruction (see Jiang and Shu [21] for the detail) in local characteristic variables. We first transform the conservative variables to the characteristic variables and then use the third-order WENO reconstruction method to reconstruct each component of the characteristic variables. The final values are obtained by transforming back to the conservative variables. Notice that the Jacobian matrix of (1) and (6) with respect to \mathbf{Q} is

$$\mathbf{J} = \begin{bmatrix} 0 & 1 & 0 & 0 \\ -u^2 + \frac{\partial p}{\partial \rho} + \Gamma \left(\frac{u^2}{2} - e \right) & u(2 - \Gamma) & \Gamma & -1 \\ \left(\Gamma \left(\frac{u^2}{2} - e \right) - e + \frac{\sigma_x}{\rho} + \frac{\partial p}{\partial \rho} \right) u & -\Gamma u^2 - \frac{\sigma_x}{\rho} + e & (1 + \Gamma)u & -u \\ \frac{4}{3}\mu \frac{u}{\rho} & -\frac{4}{3}\mu \frac{1}{\rho} & 0 & u \end{bmatrix}, \quad (19)$$

where $\Gamma = \frac{\Gamma_0 \rho_0}{\rho}$. Denote the left and right eigenvectors of \mathbf{J} by \mathbf{L} and \mathbf{R} . Then, the procedure for computing $\mathbf{Q}_{i+\frac{1}{2}}^\pm$ is as follows.

(1) Evaluate

$$\overline{\mathbf{q}}_i = \mathbf{L}(\overline{\mathbf{Q}}_i^n) \cdot \overline{\mathbf{Q}}_i^n, \quad i = -2, \dots, N+2.$$

(2) Given $\overline{\mathbf{q}}_i$, $i = -2, \dots, N+2$, use the third-order WENO reconstruction method to approximate \mathbf{q} at the cell interface, $\mathbf{q}_{i+\frac{1}{2}}^\pm$, $i = 0, \dots, N$.

(3) Evaluate

$$\mathbf{Q}_{i+\frac{1}{2}}^- = \mathbf{R}(\overline{\mathbf{Q}}_i^n) \cdot \mathbf{q}_{i+\frac{1}{2}}^-, \quad \mathbf{Q}_{i-\frac{1}{2}}^+ = \mathbf{R}(\overline{\mathbf{Q}}_i^n) \cdot \mathbf{q}_{i-\frac{1}{2}}^+, \quad i = 0, \dots, N.$$

Having obtained $\mathbf{Q}_{i+\frac{1}{2}}^\pm$ and letting $\mathbf{Q}_L = \mathbf{Q}_{i+\frac{1}{2}}^-$ and $\mathbf{Q}_R = \mathbf{Q}_{i+\frac{1}{2}}^+$, we have the Riemann problem

$$\begin{cases} \frac{\partial}{\partial t} \mathbf{U} + \frac{\partial}{\partial x} \mathbf{F}(\mathbf{U}) = 0, \\ \frac{\partial}{\partial t} s_{xx} + u \frac{\partial}{\partial x} s_{xx} = \frac{3}{4} \mu \frac{\partial}{\partial x} u, \\ \mathbf{Q}(x, 0) = \begin{cases} \mathbf{Q}_L, & \text{for } x < x_{i+\frac{1}{2}} \\ \mathbf{Q}_R, & \text{for } x > x_{i+\frac{1}{2}}. \end{cases} \end{cases} \quad (20)$$

The structure of the solution to this Riemann problem is sketched in Fig. 1. It consists of three waves corresponding to three eigenvalues ($\frac{dx}{dt} = u_L - c_L, u^*, u_R + c_R$), where

$$c = \sqrt{a^2 - \frac{\rho_0}{\rho^2} \Gamma_0 s_{xx} + \frac{4\mu}{3\rho}}, \quad a^2 = \frac{\partial p}{\partial \rho} + \frac{p}{\rho^2} \frac{\partial p}{\partial e} = a_0^2 \frac{\partial f}{\partial \eta} + \frac{p}{\rho^2} \rho_0 \Gamma_0, \quad f = \frac{(\eta - 1) [\eta - \Gamma_0(\eta - 1)/2]}{[\eta - s(\eta - 1)]^2}.$$

$\frac{dx}{dt} = u^*$ corresponds to the contact wave while $\frac{dx}{dt} = u_L - c_L$ and $\frac{dx}{dt} = u_R + c_R$ correspond to the left-going and right-going waves, respectively. These three waves separate four constant states. From left to right, they are \mathbf{Q}_L (left data state), \mathbf{Q}_L^* , \mathbf{Q}_R^* , and \mathbf{Q}_R (right data state). TRRSE [11] is used to obtain \mathbf{Q}_L^* and \mathbf{Q}_R^* . Have obtained $\mathbf{Q}_L, \mathbf{Q}_L^*, \mathbf{Q}_R^*,$ and \mathbf{Q}_R , we define the Godunov values of \mathbf{Q} as

$$\mathbf{Q}_{i+\frac{1}{2}} = \begin{cases} \mathbf{Q}_L, & \text{for } \dot{x} \leq u_L - c_L \\ \mathbf{Q}_L^*, & \text{for } u_L - c_L < \dot{x} \leq u^* \\ \mathbf{Q}_R^*, & \text{for } u^* < \dot{x} \leq u_R + c_R \\ \mathbf{Q}_R, & \text{for } \dot{x} > u_R + c_R. \end{cases} \quad (21)$$

Note that the effects of mesh movement (at the speed of $\dot{x} = u - w$) has been taken into consideration.

The Godunov values of $\rho, u, p,$ and s_{xx} can then be obtained from $\mathbf{Q}_{i+\frac{1}{2}}$. After that, the numerical flux can be computed using (18) for the conservative equations (1). It is noted that we have $u^* = u_L^* = u_R^*$ by the construction of TRRSE [11].

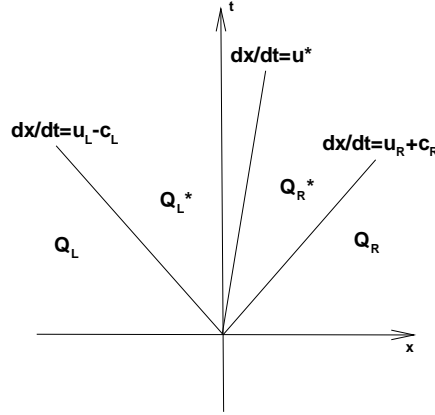


Figure 1: A sketch of the solution structure of the Riemann problem (20).

We now discuss the spatial discretization of the constitutive equation. Notice that the equation of the constitute model (6) can be written as

$$\left(\frac{ds_{xx}}{dt} \right)_{\dot{x}} = \frac{4\mu}{3} \frac{\partial u}{\partial x} - w \frac{\partial s_{xx}}{\partial x}, \quad (22)$$

where the left-hand side stands for the time derivative of s_{xx} along the mesh trajectories. We discretize $\frac{\partial u}{\partial x}$ in cell I_i by

$$\frac{\partial u}{\partial x} \approx \frac{u_{i+\frac{1}{2}} - u_{i-\frac{1}{2}}}{x_{i+\frac{1}{2}} - x_{i-\frac{1}{2}}}. \quad (23)$$

Moreover, $w \frac{\partial s_{xx}}{\partial x}$ can be discretized as

$$\begin{aligned} w \frac{\partial s_{xx}}{\partial x} &= \frac{\partial w s_{xx}}{\partial x} - s_{xx} \frac{\partial w}{\partial x} \\ &\approx \frac{w_{i+\frac{1}{2}} s_{xx,i+\frac{1}{2}} - w_{i-\frac{1}{2}} s_{xx,i-\frac{1}{2}}}{\Delta x_i} - (\overline{s_{xx}})_i \frac{w_{i+\frac{1}{2}} - w_{i-\frac{1}{2}}}{\Delta x_i}. \end{aligned} \quad (24)$$

Combining the above approximations, we get

$$\frac{ds_{xx}}{dt} = \frac{4\mu}{3} \frac{u_{i+\frac{1}{2}} - u_{i-\frac{1}{2}}}{x_{i+\frac{1}{2}} - x_{i-\frac{1}{2}}} - \frac{w_{i+\frac{1}{2}} s_{xx,i+\frac{1}{2}} - w_{i-\frac{1}{2}} s_{xx,i-\frac{1}{2}}}{\Delta x_i} + (\overline{s_{xx}})_i \frac{w_{i+\frac{1}{2}} - w_{i-\frac{1}{2}}}{\Delta x_i}, \quad (25)$$

where $u_{i\pm\frac{1}{2}}$ and $s_{xx,i\pm\frac{1}{2}}$ are the Godunov values of u and s_{xx} at the left and right boundaries of I_i , respectively.

The semi-discrete scheme (17) and (25) and the von Mises yielding condition (7) are integrated using a third-order TVD Runge-Kutta method. Notice that the mesh changes with time, the node location and the cell size need to be updated at each Runge-Kutta stage. Moreover, the relative velocity w is kept constant in time for this time step. The scheme reads as follows.

Stage 1.

$$\begin{aligned} x_{i+\frac{1}{2}}^{(1)} &= x_{i+\frac{1}{2}}^{(0)} + \Delta t^n \left(u_{i+\frac{1}{2}}^n - w_{i+\frac{1}{2}} \right), \\ \Delta x_i^{(1)} &= x_{i+\frac{1}{2}}^{(1)} - x_{i-\frac{1}{2}}^{(1)}, \\ \Delta x_i^{(1)} \overline{\mathbf{U}}_i^{(1)} &= \Delta x_i^{(0)} \overline{\mathbf{U}}_i^{(0)} + \Delta t^n \mathcal{L} \left(\overline{\mathbf{U}}_i^{(0)}, (\overline{s_{xx}})_i^{(0)}, x_{i+\frac{1}{2}}^{(0)}, w_{i+\frac{1}{2}} \right), \\ (\overline{s_{xx}})_i^{(1)} &= (\overline{s_{xx}})_i^{(0)} + \Delta t^n \Theta \left(u_{i+\frac{1}{2}}^{(0)}, (\overline{s_{xx}})_i^{(0)}, x_{i+\frac{1}{2}}^{(0)}, w_{i+\frac{1}{2}} \right), \\ (\overline{s_{xx}})_i^{(1)} &= \Upsilon((\overline{s_{xx}})_i^{(1)}); \end{aligned}$$

Stage 2.

$$\begin{aligned} x_{i+\frac{1}{2}}^{(2)} &= \frac{3}{4} x_{i+\frac{1}{2}}^{(0)} + \frac{1}{4} \left[x_{i+\frac{1}{2}}^{(1)} + \Delta t^n \left(u_{i+\frac{1}{2}}^{(1)} - w_{i+\frac{1}{2}} \right) \right], \\ \Delta x_i^{(2)} &= x_{i+\frac{1}{2}}^{(2)} - x_{i-\frac{1}{2}}^{(2)}, \\ \Delta x_i^{(2)} \overline{\mathbf{U}}_i^{(2)} &= \frac{3}{4} \Delta x_i^{(0)} \overline{\mathbf{U}}_i^{(0)} + \frac{1}{4} \left[\Delta x_i^{(1)} \overline{\mathbf{U}}_i^{(1)} + \Delta t^n \mathcal{L} \left(\overline{\mathbf{U}}_i^{(1)}, (\overline{s_{xx}})_i^{(1)}, x_{i+\frac{1}{2}}^{(1)}, w_{i+\frac{1}{2}} \right) \right], \\ (\overline{s_{xx}})_i^{(2)} &= \frac{3}{4} (\overline{s_{xx}})_i^{(0)} + \frac{1}{4} \left[(\overline{s_{xx}})_i^{(1)} + \Delta t^n \Theta \left(u_{i+\frac{1}{2}}^{(1)}, (\overline{s_{xx}})_i^{(1)}, x_{i+\frac{1}{2}}^{(1)}, w_{i+\frac{1}{2}} \right) \right], \\ (\overline{s_{xx}})_i^{(2)} &= \Upsilon((\overline{s_{xx}})_i^{(2)}); \end{aligned}$$

Stage 3.

$$\begin{aligned}
x_{i+\frac{1}{2}}^{(3)} &= \frac{1}{3}x_{i+\frac{1}{2}}^{(0)} + \frac{2}{3} \left[x_{i+\frac{1}{2}}^{(2)} + \Delta t^n \left(u_{i+\frac{1}{2}}^{(2)} - w_{i+\frac{1}{2}} \right) \right], \\
\Delta x_i^{(3)} &= x_{i+\frac{1}{2}}^{(3)} - x_{i-\frac{1}{2}}^{(3)}, \\
\Delta x_i^{(3)} \overline{\mathbf{U}}_i^{(3)} &= \frac{1}{3} \Delta x_i^{(0)} \overline{\mathbf{U}}_i^{(0)} + \frac{2}{3} \left[\Delta x_i^{(2)} \overline{\mathbf{U}}_i^{(2)} + \Delta t^n \mathcal{L} \left(\overline{\mathbf{U}}_i^{(2)}, (\overline{sxx})_i^{(2)}, x_{i+\frac{1}{2}}^{(2)}, w_{i+\frac{1}{2}} \right) \right], \\
(\overline{sxx})_i^{(3)} &= \frac{1}{3} (\overline{sxx})_i^{(0)} + \frac{2}{3} \left[(\overline{sxx})_i^{(2)} + \Delta t^n \Theta \left(u_{i+\frac{1}{2}}^{(2)}, (\overline{sxx})_i^{(2)}, x_{i+\frac{1}{2}}^{(2)}, w_{i+\frac{1}{2}} \right) \right], \\
(\overline{sxx})_i^{(3)} &= \Upsilon((\overline{sxx})_i^{(3)}).
\end{aligned}$$

Here, \mathcal{L} and Θ are the spatial operators representing the right-hand sides of (17) and (25), respectively, and

$$\begin{aligned}
x_{i+\frac{1}{2}}^{(0)} &= x_{i+\frac{1}{2}}^n, & x_{i+\frac{1}{2}}^{n+1} &= x_{i+\frac{1}{2}}^{(3)}, & u_{i+\frac{1}{2}}^{(0)} &= u_{i+\frac{1}{2}}^n, & u_{i+\frac{1}{2}}^{n+1} &= u_{i+\frac{1}{2}}^{(3)}, \\
\Delta x_i^{(0)} &= \Delta x_i^n, & \Delta x_i^{n+1} &= \Delta x_i^{(3)}, & \overline{\mathbf{U}}_i^{(0)} &= \overline{\mathbf{U}}_i^n, & \overline{\mathbf{U}}_i^{n+1} &= \overline{\mathbf{U}}_i^{(3)}, \\
(\overline{sxx})_i^{(0)} &= (\overline{sxx})_i^n, & (\overline{sxx})_i^{n+1} &= (\overline{sxx})_i^{(3)}, \\
\Upsilon(\beta) &= \begin{cases} \beta, & \text{for } |\beta| \leq \frac{2}{3}Y_0 \\ \frac{2}{3}Y_0, & \text{for } \beta > \frac{2}{3}Y_0 \\ -\frac{2}{3}Y_0, & \text{for } \beta < -\frac{2}{3}Y_0. \end{cases} \tag{26}
\end{aligned}$$

Recall from Section 3.1 that for the free boundary points, we have $w_{\frac{1}{2}} = w_{N+\frac{1}{2}} = 0$ by construction. Then, at these points the above scheme reduces to

$$\begin{aligned}
x_{i+\frac{1}{2}}^{(1)} &= x_{i+\frac{1}{2}}^{(0)} + \Delta t^n u_{i+\frac{1}{2}}^n, & i &= 0, N \\
x_{i+\frac{1}{2}}^{(2)} &= \frac{3}{4}x_{i+\frac{1}{2}}^{(0)} + \frac{1}{4} \left[x_{i+\frac{1}{2}}^{(1)} + \Delta t^n u_{i+\frac{1}{2}}^{(1)} \right], & i &= 0, N \\
x_{i+\frac{1}{2}}^{(3)} &= \frac{1}{3}x_{i+\frac{1}{2}}^{(0)} + \frac{2}{3} \left[x_{i+\frac{1}{2}}^{(2)} + \Delta t^n u_{i+\frac{1}{2}}^{(2)} \right], & i &= 0, N
\end{aligned}$$

which is exactly the third-order Runge-Kutta scheme applied to the Lagrangian movement $\dot{x} = u$.

3.4 Time step size

The time step size Δt^n is determined using the CFL condition

$$\Delta t^n = 0.45 \min_{i=1, \dots, N} \left(\frac{\Delta x_i^n}{c_i^n + |w_i|} \right),$$

where c_i^n is the sound speed of solid in cell I_i at t^n , and $w_i = \frac{1}{2}(w_{i+\frac{1}{2}} + w_{i-\frac{1}{2}})$.

4 Numerical examples

In this section we present three numerical examples to verify the convergence order of the MMCC scheme described in the previous section and its ability to capture elastic-plastic waves.

4.1 Accuracy test

We use smooth solutions to verify the accuracy of the MMCC scheme. The initial condition is chosen as

$$\rho(x, 0) = \rho_0 - 0.1 \sin(2\pi x), \quad u(x, 0) = 1 - 0.01 \sin(2\pi x), \quad p = 2, \quad s_{xx} = 0.$$

The initial domain is $(0, 1)$, and both ends of the domain move at the flow velocity. A periodic boundary condition is used. The EOS is given by the Mie-Grüneisen model with parameters $\rho_0 = 8930 \text{ kg/m}^3$, $a_0 = 3940 \text{ m/s}$, $\Gamma_0 = 2$, and $s = 1.49$. The constitutive model is characterized by the shear module $\mu = 4.5 \times 10^9 \text{ Pa}$ and the yield strength $Y^0 = 90 \times 10^9 \text{ Pa}$. There is no exact solution for this problem. The reference solution is obtained using the third order cell-centered Lagrangian scheme [11] with a uniform mesh of 4000 points.

The MMCC scheme is applied to the problem up to $t = 1$. The L_1 - and L_2 -norms of the error at the final time $t = 1$ are shown in Tables 1 and 2. The results confirm the anticipated third-order accuracy of the MMCC scheme.

Table 1: The L_1 -norm of the error for the MMCC scheme for the smooth solutions.

N	ρ	Order	ρu	Order	ρE	Order	s_{xx}	Order
50	1.229E-03	-	1.680E-03	-	1.587E-03	-	7.685E-05	-
100	4.408E-04	1.48	4.260E-04	1.98	3.451E-04	2.20	2.540E-05	1.60
200	7.900E-05	2.48	7.430E-05	2.52	5.784E-05	2.58	4.241E-06	2.58
400	1.054E-05	2.91	9.737E-06	2.93	6.914E-06	3.06	4.366E-07	3.28

Table 2: The L_2 -norm of the error for the MMCC scheme for the smooth solutions.

N	ρ	Order	ρu	Order	ρE	Order	s_{xx}	Order
50	1.414E-03	-	2.187E-03	-	2.095E-03	-	8.911E-05	-
100	5.148E-04	1.46	5.852E-04	1.90	5.104E-04	2.04	3.276E-05	1.44
200	1.028E-04	2.32	1.164E-04	2.33	9.902E-05	2.37	6.068E-06	2.43
400	1.534E-05	2.74	1.681E-05	2.79	1.302E-05	2.93	7.097E-07	3.10

4.2 A piston problem with stress shock waves in copper

This piston problem is concerned with a piece of copper with the following initial setting: the length of copper is 1 m , the initial density $\rho_0 = 8930 \text{ kg/m}^3$, the initial pressure $p_0 = 10^5 \text{ Pa}$, and the initial velocity is zero. The EOS for copper is given by the Mie-Grüneisen model with parameters $\rho_0 = 8930 \text{ kg/m}^3$, $a_0 = 3940 \text{ m/s}$, $\Gamma_0 = 2$, and $s = 1.49$. The constitutive model is characterized by the shear module $\mu = 45 \times 10^9 \text{ Pa}$ and the yield strength $Y^0 = 90 \times 10^6 \text{ Pa}$. A velocity boundary condition

$v_{piston} = 20m/s$ is used on the left free boundary while the wall boundary condition is implemented on the right fixed boundary. This problem has an exact solution; see [25].

To show the convergence of the MMCC scheme, we solve the problem with 100, 200, and 400 cells. The final time is $t = 150\mu s$. The numerical results with different N are shown in Figs. 2 and 3. From the figures we can see that the numerical solution is getting closer to the exact solution for larger N . Moreover, the scheme well captures the plastic shock wave (near $x = 0.6$) and the elastic shock wave (near $x = 0.7$) and there is no numerical oscillation near the shock waves. Furthermore, the yielding condition (7) is in effect for $0 < x < 0.7$ (cf. Fig. 3). It creates the plastic shock wave and also makes s_{xx} to be only piecewise smooth. The L_1 - norm of the error at the final time $t = 150\mu s$ are shown in Table 3. Due to the discontinuity of the exact solution at the elastic shock wave and its non-smoothness at the plastic shock wave, the scheme cannot be expected to converge at the optimal third-order rate. The results show that the convergence is about first order for this problem as the mesh is refined.

We also compare the MMCC scheme with the third-order cell-centered Lagrangian scheme (CCL) based on the same Riemann solver TRRSE of [11]. The comparison results are shown in Fig. 4. We can see that MMCC is more accurate than CCL especially around the shock waves. This is due to the fact that MMCC concentrates more points around the shock waves; see the mesh trajectories shown in Fig. 5. No mesh crossing has been experienced for all of the computation for this example.

Table 3: The L_1 -norm of the error for the MMCC scheme for the piston problem.

N	ρ	Order	ρu	Order	ρE	Order	s_{xx}	Order
100	6.732E-04	-	2.783E-04	-	7.429E-07	-	1.038E-05	-
200	2.871E-04	1.23	1.195E-04	1.22	3.817E-07	0.96	4.924E-06	1.08
400	1.249E-04	1.20	5.207E-05	1.20	1.856E-07	1.04	2.316E-06	1.09

4.3 Wilkins' problem with the Mie-Grüneisen EOS

This problem, originally introduced by Wilkins [35], is used here to show the ability of the MMCC scheme to compute rarefaction waves. It describes a moving aluminium plate striking on another aluminium plate. The EOS for aluminium is the Mie-Grüneisen model with parameters $\rho_0 = 2785kg/m^3$, $a_0 = 5328m/s$, $\Gamma_0 = 2$, and $s = 1.338$. The constitutive model is characterized by the shear module $\mu = 27.6 \times 10^9 Pa$ and the yield strength $Y^0 = 300 \times 10^6 Pa$. The initial condition of this problem is

$$(\rho, u, p) = \begin{cases} (2785kg/m^3, 800m/s, 10^{-6}Pa), & \text{for } 0m \leq x \leq 5 \times 10^{-3}m, \\ (2785kg/m^3, 0m/s, 10^{-6}Pa), & \text{for } 5 \times 10^{-3}m \leq x \leq 50 \times 10^{-3}m. \end{cases} \quad (27)$$

We use 200, 400, and 800 cells to solve the problem up to $t = 5\mu s$ with a free boundary condition on the left boundary and the wall boundary condition on the right boundary. Computed results are presented in Figs. 6 to 9. The reference solution (solid lines in all figures) is computed by the third-order cell-centered Lagrangian scheme based on HLLCE Riemann solvers given in [10] using 4000 cells.

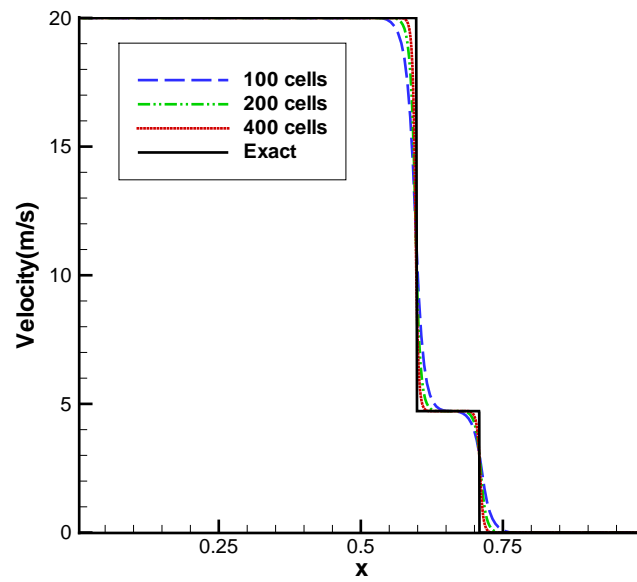
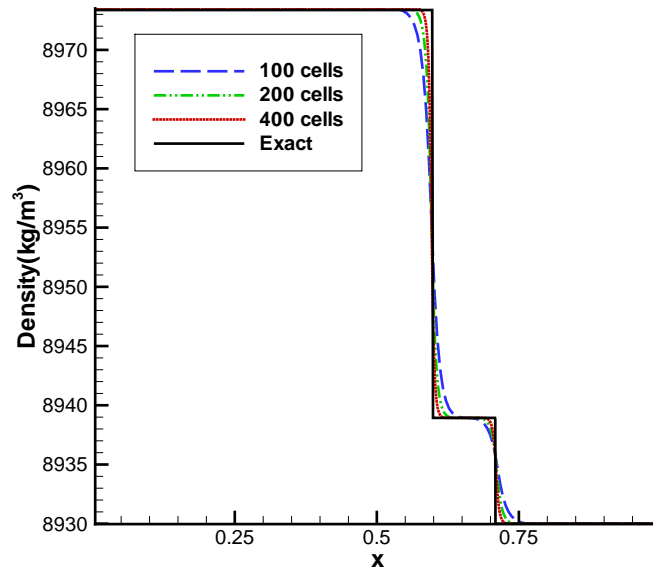


Figure 2: Piston problem. The density and velocity at $t = 150\mu s$ are shown.

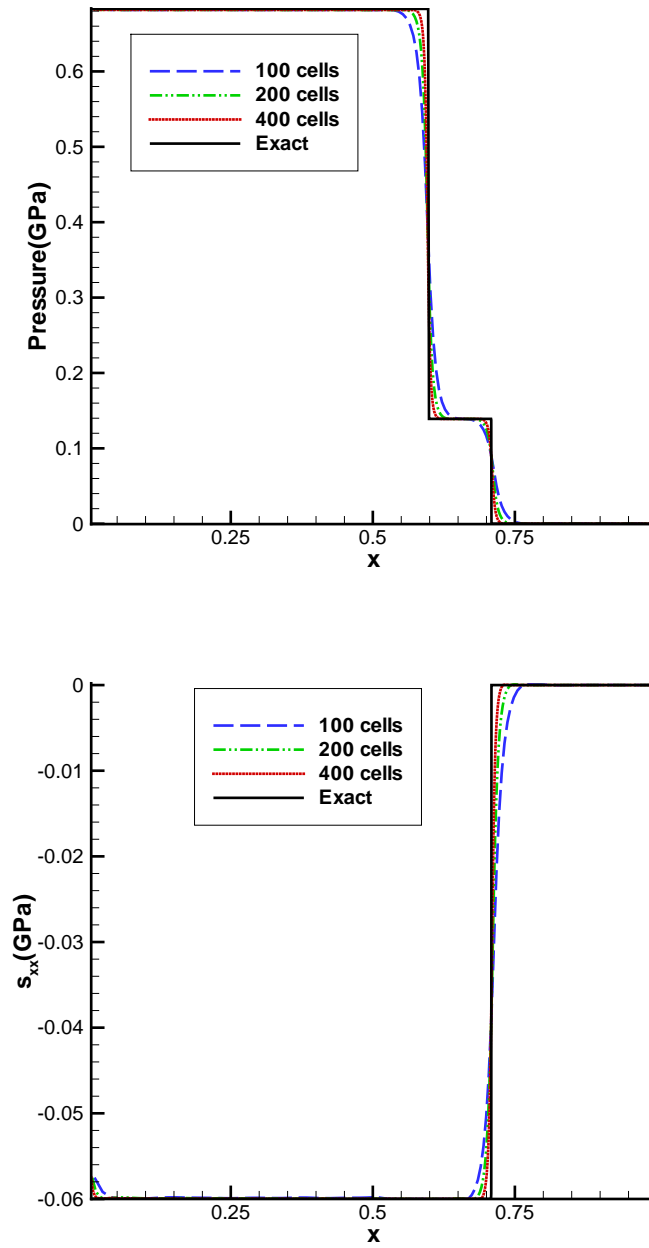


Figure 3: Piston problem. The pressure and s_{xx} at $t = 150\mu s$ are shown.

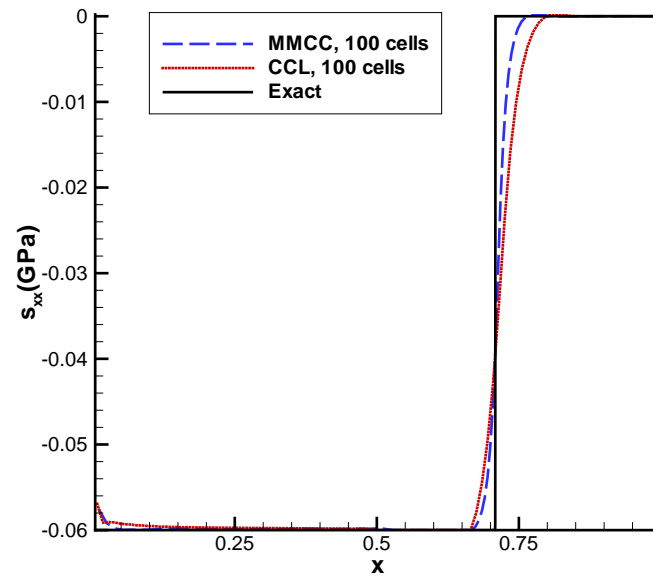
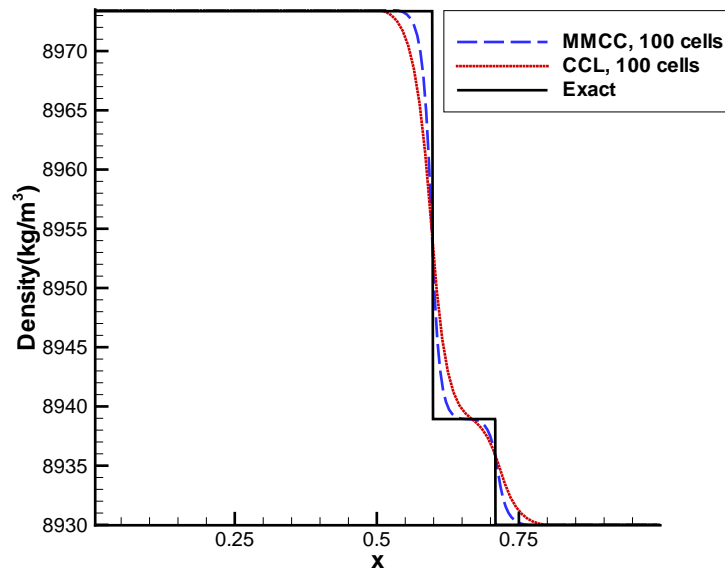


Figure 4: Piston problem. The density and s_{xx} are shown for MMCC and CCL schemes with 100 cells.

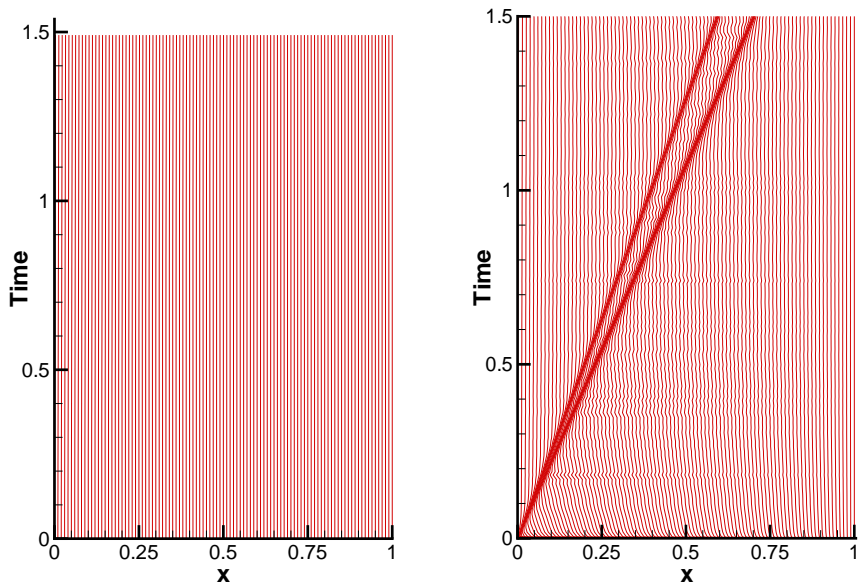


Figure 5: Piston problem. Mesh trajectories for CCL (left) and MMCC (right) schemes with 100 cells.

From Figs. 6 to 9 we can observe that the numerical solution converges to the reference one as the number of cells increases. Moreover, the elastic and plastic right-facing shocks and the reflected elastic and plastic rarefaction waves are resolved well. These results are in good agreement with those in [10].

We also compare the numerical results of MMCC and CCL in Fig. 10. One can see that MMCC is more accurate than CCL for both shock and rarefaction waves. Interestingly, the improvements are significant for the shock waves (between $3.4 < x < 4$) and the reflected elastic rarefaction wave (between $3 < x < 3.2$) whereas that for the plastic rarefaction wave is only marginal. This is reflected in the mesh concentration; see the mesh trajectories in Fig. 11. To explain this, we recall that the monitor function (14) is defined in terms of the first derivatives of ρ and s_{xx} . The density changes abruptly in the shock wave regions while varying only gradually in the rarefaction wave regions. Moreover, the flow in the regions of both plastic shock and rarefaction waves is plastic, and from the von Mises yielding condition (cf. (7) and (26)), s_{xx} remains constant and its derivative is zero in these regions. Consequently, the derivative of s_{xx} is more significant in the regions of elastic (shock and rarefaction) waves than in the regions of plastic waves. By combining the behavior of both ρ and s_{xx} and from the definition of the monitor function, we know that the monitor function and therefore the mesh concentration are large around the (elastic and plastic) shock waves and the elastic rarefaction waves. On the other hand, the current definition of the monitor function leads to a relatively low mesh concentration and only a marginal improvement in accuracy with MMCC over CCL around the plastic rarefaction wave. Unfortunately, it is unclear to the authors how to concentrate more mesh points in the regions of plastic rarefaction waves in an automatic manner. This will be an interesting

topic for future research.

Overall, we have seen that MMCC is more accurate than CCL and is effective in concentrating the mesh points around the shock and elastic rarefaction waves. No mesh crossing has been experienced for this example too.

5 Conclusions

In the previous sections a third-order moving mesh cell-centered scheme has been developed for the numerical solution of one-dimensional elastic-plastic flows with the Mie-Grüneisen equation of state, the Wilkins constitutive model, and the von Mises yielding criterion. The scheme moves and adapts the mesh by combining the Lagrangian method with the MMPDE moving mesh method. The goal is to take advantages of both methods to better resolve shock and other types of waves and be more robust in preventing the mesh from crossing and tangling. Moreover, the MMCC scheme treats the relative velocity of the flow with respect to the mesh as constant in time between time steps. An advantage of this treatment is that free boundaries can be approximated with high-order accuracy. This is different from many existing moving mesh methods where the mesh velocity is treated as constant, which gives a second-order approximation of free boundaries. Furthermore, a time dependent scaling is used in the computation of the monitor function to avoid possible sudden movement of the mesh points due to the creation or diminishing of shock and rarefaction waves or the steepening of those waves. Finally, the two-rarefaction Riemann solver with elastic wave (TRRSE) is used to evaluate the Godunov values of the density, pressure, velocity, and deviatoric stress at cell interfaces and no remapping is used.

The third-order accuracy of the scheme has been verified for a smooth problem with Wilkins' constitutive model. The MMCC scheme has also been used for the piston and Wilkins' problems. The numerical tests have demonstrated the convergence of the scheme and its ability to concentrate mesh points around shock and elastic rarefaction waves while the obtained numerical results are in good agreement with those in literature. Comparison studies have shown that MMCC is more accurate in resolving shock waves and rarefaction waves than the CCL (Lagrangian mesh) scheme. It is also worth mentioning that no mesh crossing has been experienced in the computation for all three examples.

Finally, it is pointed out that the focus of the current work is on one-dimensional problems. Nevertheless, since both the cell-centered Lagrangian and MMPDE moving mesh methods are known to work well in multi-dimensions, we believe that the MMCC scheme should be able to extend to multi-dimensional elastic-plastic flows without major modifications. Investigations for such an extension are underway.

Acknowledgments. This work was partially supported by NSFC (China) (Grant No. 11172050, 11672047, and 11272064), the National Basic Research Program (China) (Grant No. 2014CB745002), and Science Challenge Project (Grant No. TZ2016002). The authors are grateful to the anonymous referees for their valuable comments in improving the quality of the paper.

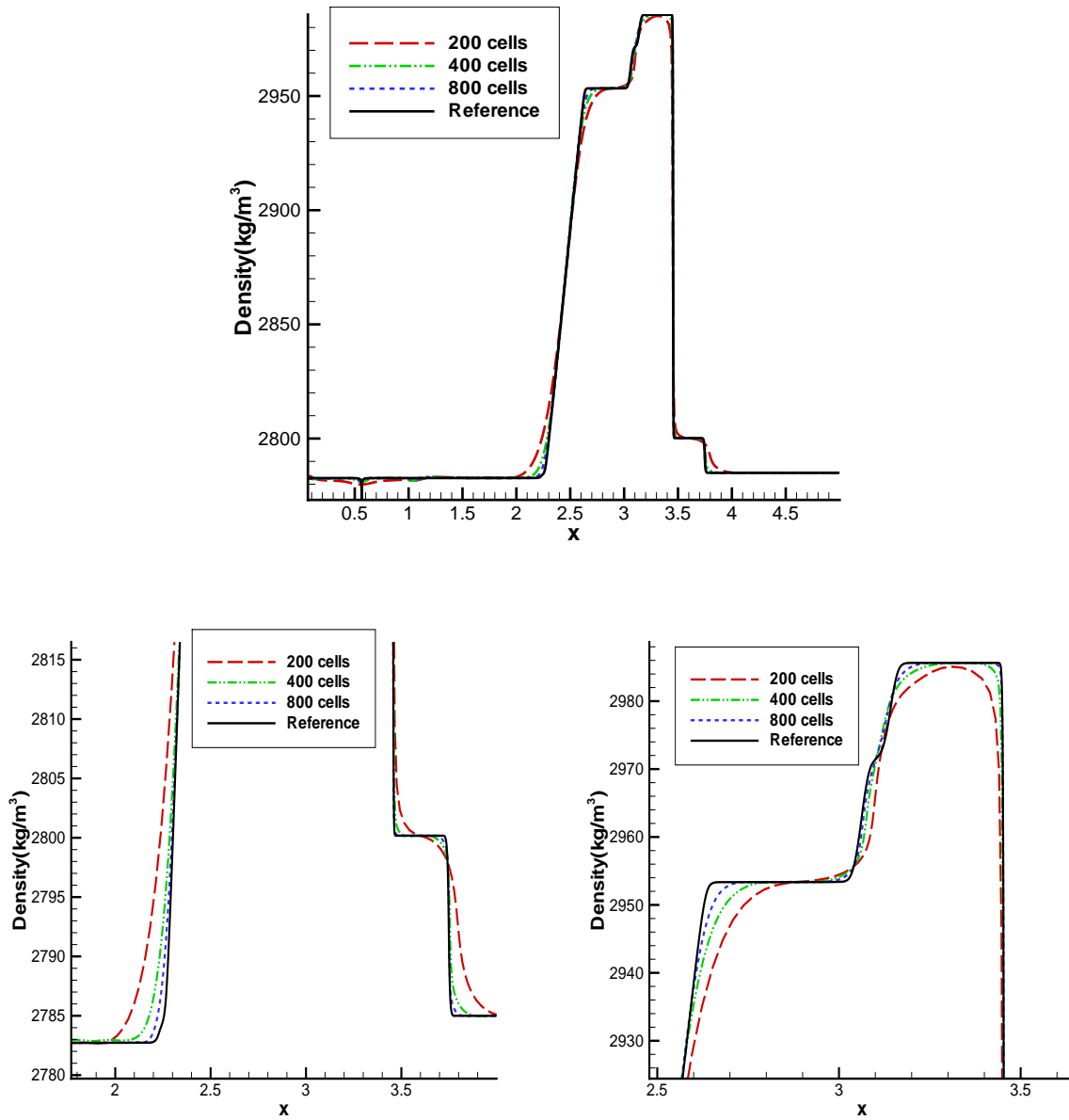


Figure 6: Wilkins' problem with the Mie-Grüneisen EOS. The density at time $t = 5\mu\text{s}$ is shown. The bottom figures are the close-up of the regions around the rarefaction and shock waves.

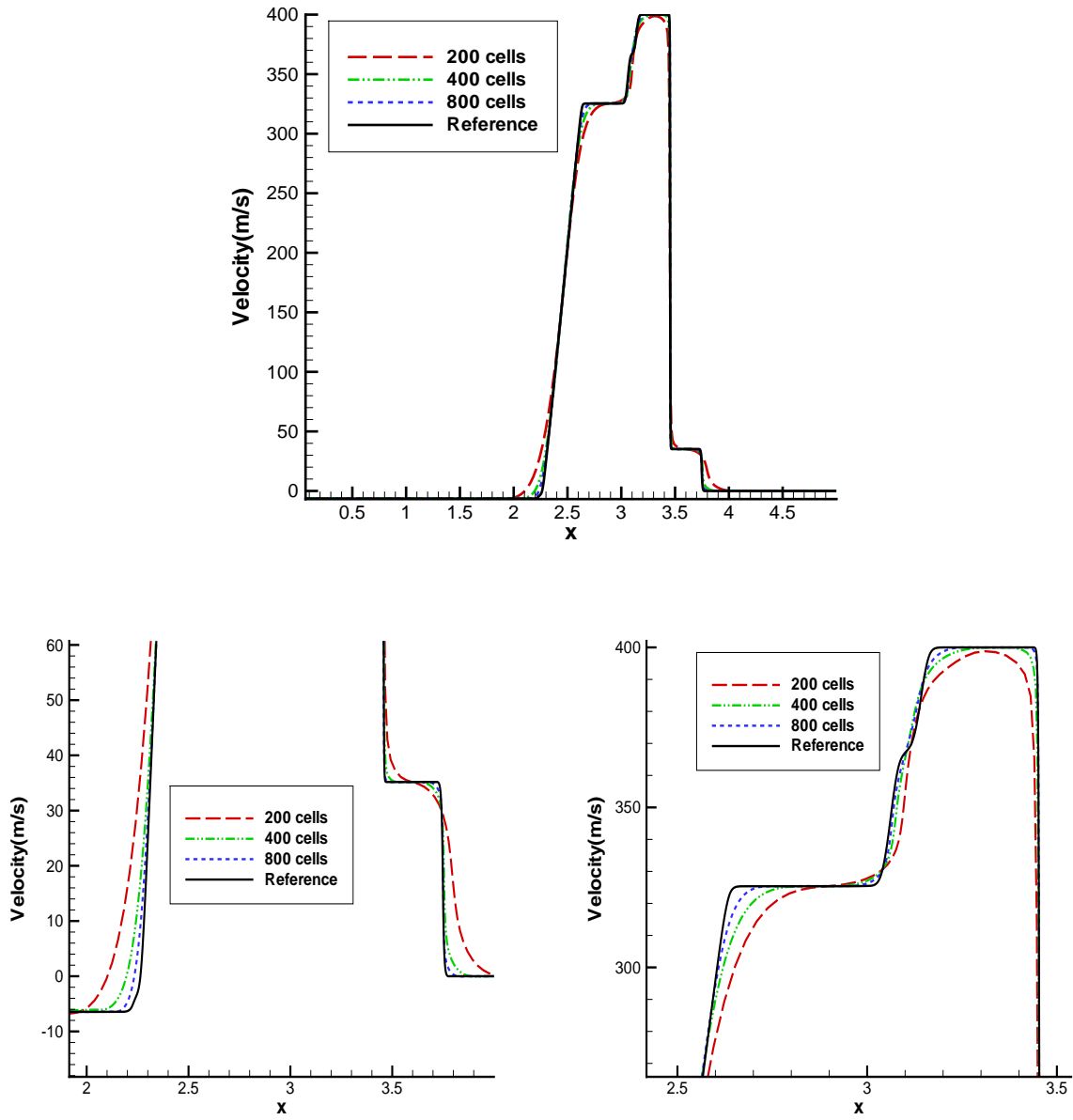


Figure 7: Wilkins' problem with the Mie-Grüneisen EOS. The velocity at $t = 5\mu s$ is shown. The bottom figures are the close-up of the regions around the rarefaction and shock waves.

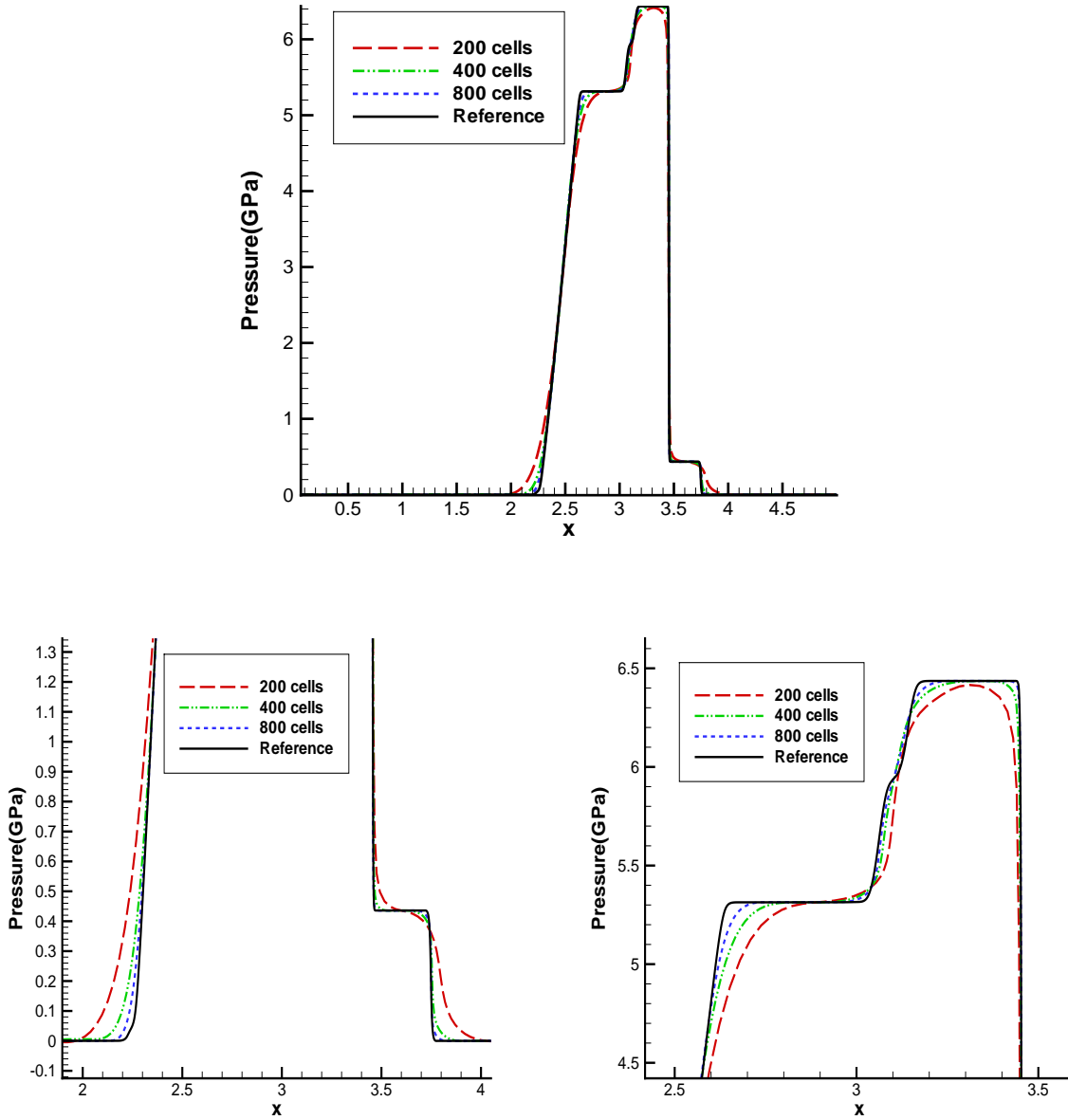


Figure 8: Wilkins' problem with the Mie-Grüneisen EOS. The pressure at $t = 5\mu s$ is shown. The bottom figures are the close-up of the regions around the rarefaction and shock waves.

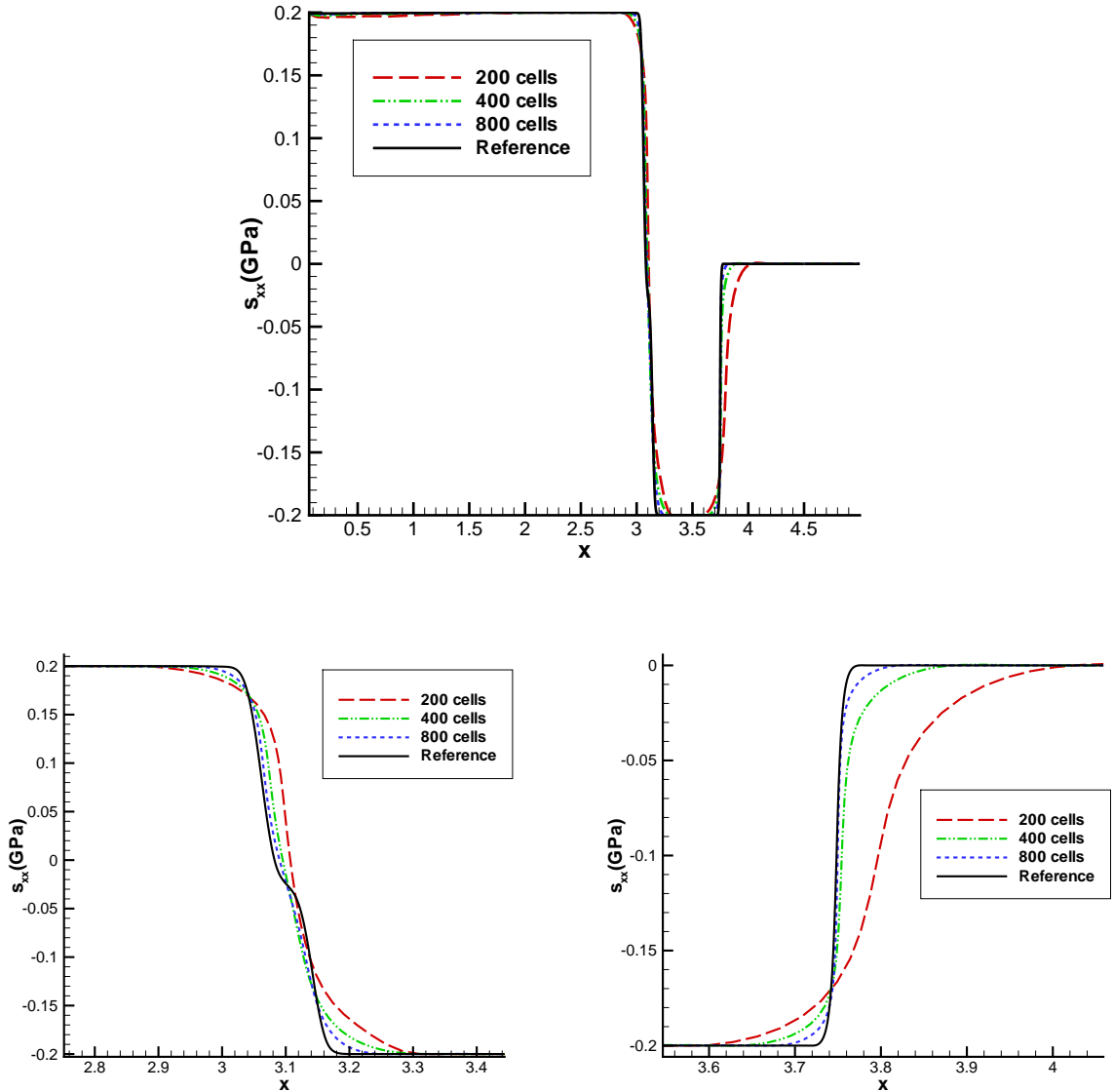


Figure 9: Wilkins' problem with the Mie-Grüneisen EOS. s_{xx} at $t = 5\mu s$ is shown. The bottom figures are the close-up of the region around the right-facing elastic shock wave.

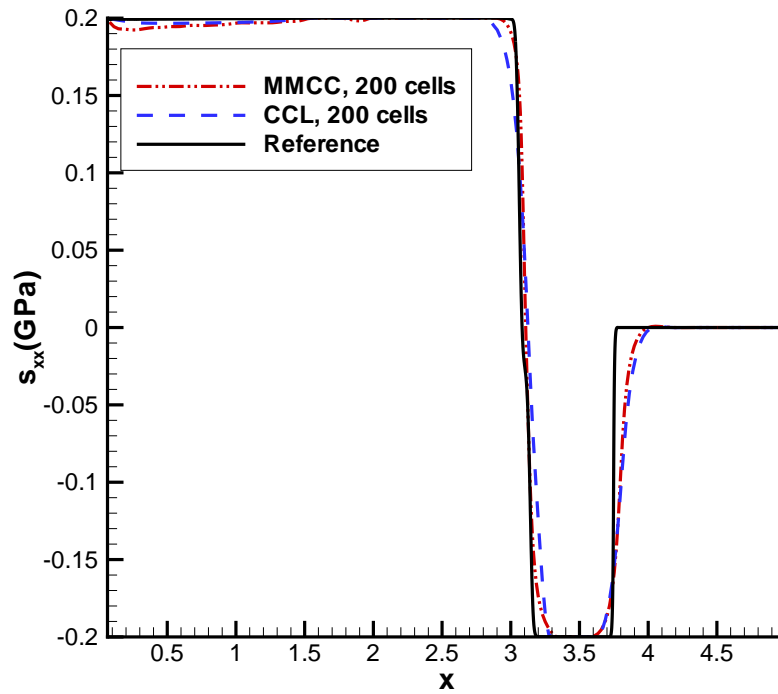
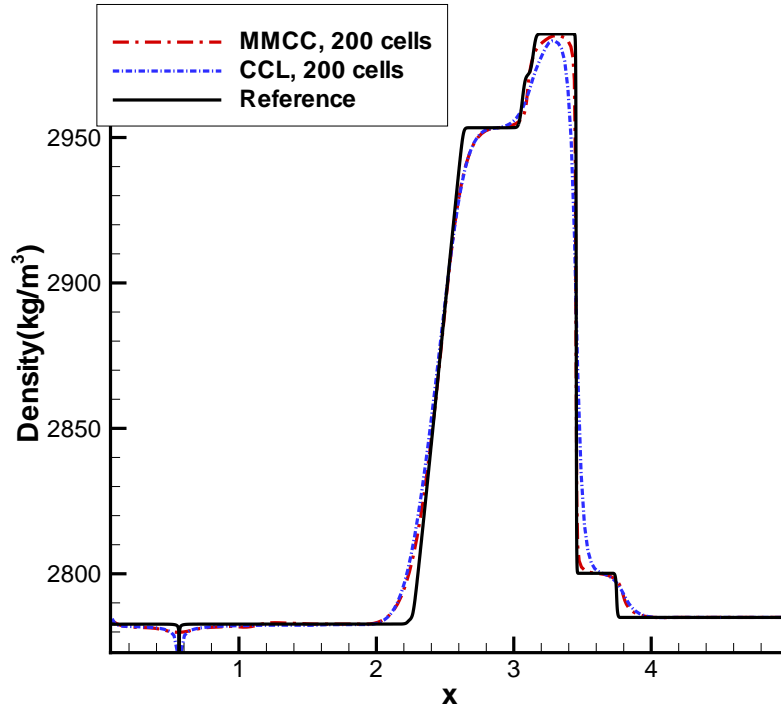


Figure 10: Wilkins' problem with the Mie-Grüneisen EOS. The density and s_{xx} are shown for MMCC and CCL with 200 cells.

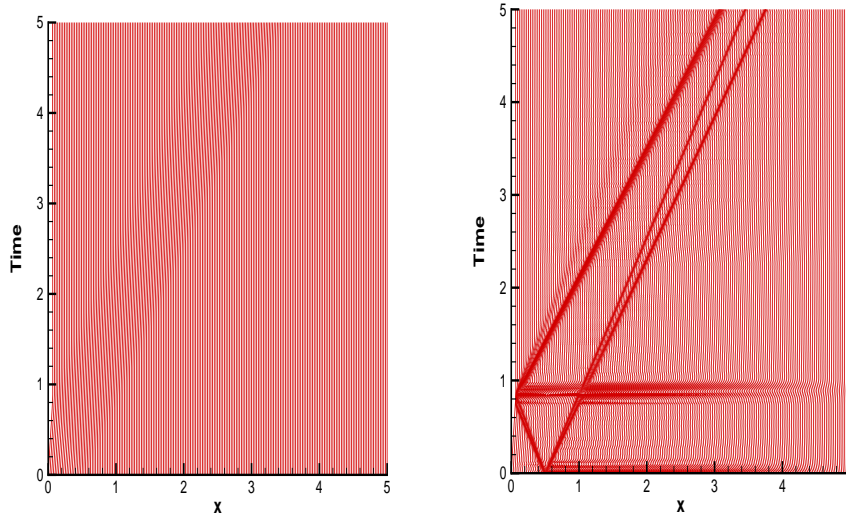


Figure 11: Wilkins' problem. The mesh trajectories for CCL (left) and MMCC (right) schemes with 400 cells.

References

- [1] M. J. Baines. *Moving Finite Elements*. Oxford University Press, Oxford, 1994.
- [2] M. J. Baines, M. E. Hubbard, and P. K. Jimack, A moving mesh finite element algorithm for the adaptive solution of time-dependent partial differential equations with moving boundaries. *Appl. Numer. Math.* 54 (2005), 450-469.
- [3] M. J. Baines, M. E. Hubbard, and P. K. Jimack. Velocity-based moving mesh methods for nonlinear partial differential equations. *Commun. Comput. Phys.* 10 (2011), 509-576.
- [4] P. T. Barton, D. Drikakis, E. Romenski1, and V. A. Titarev, Exact and approximate solutions of Riemann problems in non-linear elasticity. *J. Comput. Phys.* 228 (2009), 7046-7068.
- [5] W. Boscheri, M. Dumbser, and D. S. Balsara, High-order ADER-WENO ALE schemes on unstructured triangular meshes – application of several node solvers to hydrodynamics and magneto-hydrodynamics, *Int. J. Numer. Meth. Fluids* 76 (2014), 737-778.
- [6] W. Boscheri, M. Dumbser, and R. Loubère, On direct Arbitrary-Lagrangian-Eulerian ADER-WENO finite volume schemes for the HPR model of nonlinear hyperelasticity, arXiv:1602.06869.
- [7] C. J. Budd, W. Huang, and R. D. Russell, Adaptivity with moving grids, *Acta Numerica*, 18 (2009), 111–241.
- [8] C. J. Budd and J. F. Williams, Parabolic Monge-Ampère methods for blow-up problems in several spatial dimensions. *J. Phys. A Math. Gen.* 39 (2006), 5425-5444.

- [9] D. E. Burton, T. C. Carney, N. R. Morgan, S. K. Sambasivan, and M. J. Shashkov, A cell-centered Lagrangian Godunov-like method for solid dynamics. *Comput. Fluids*, 83 (2013), 33-47.
- [10] J. Cheng, A Harten-Lax-van Leer-contact (HLLC) approximation Riemann solver with elastic waves for one-dimensional elastic-plastic problems, *Appl. Math. Mech.* 37 (2016), 1517-1538.
- [11] J. Cheng, E. F. Toro, S. Jiang, M. Yu, and W. Tang, A high-order cell-centered Lagrangian scheme for one-dimensional elastic-plastic problems. *Comput. Fluids*, 122 (2015) 136-152.
- [12] D. J. Hill, D. Pullin, M. Ortiz, and D. Meiron. An Eulerian hybrid WENO centered-difference solver for elastic-plastic solids. *J. Comput. Phys.* 229 (2010), 9503-9072.
- [13] C. W. Hirt, A. A. Amsden, and J. L. Cook, An arbitrary Lagrangian-Eulerian computing method for all flow speeds, *J. Comput. Phys.* 14 (1974), 227-253.
- [14] W. Huang, Unconditionally stable high-order time integration for moving mesh finite difference solution of linear convection-diffusion equations, *Int. J. Comput. Math.* 92 (2015), 1180-1203.
- [15] W. Huang and L. Kamenski, A geometric discretization and a simple implementation for variational mesh generation and adaptation, *J. Comput. Phys.* 301 (2015), 322-337.
- [16] W. Huang and L. Kamenski, On the mesh nonsingularity of the moving mesh PDE method, *Math. Comp.* (to appear, DOI: 10.1090/mcom/3271), (arXiv:1512.04971).
- [17] W. Huang, Y. Ren, and R. D. Russell, Moving mesh methods based on moving mesh partial differential equations. *J. Comput. Phys.* 113 (1994), 279-290.
- [18] W. Huang, Y. Ren, and R. D. Russell, Moving mesh partial differential equations (MMPDEs) based upon the equidistribution principle. *SIAM J. Numer. Anal.* 31 (1994), 709-730.
- [19] W. Huang and R. D. Russell, Moving mesh strategy based upon a gradient flow equation for two dimensional problems. *SIAM J. Sci. Comput.* 20 (1999), 998-1015.
- [20] W. Huang and R. D. Russell, Adaptive Moving Mesh Methods, Springer-Verlag, New York, 2011.
- [21] G. S. Jiang and C.-W. Shu, Efficient implementation of weighted ENO schemes. *J. Comput. Phys.* 126 (1996), 202-228.
- [22] G. Kluth and B. Després, Discretization of hyperelasticity on unstructured mesh with a cell-centered Lagrangian scheme. *J. Comput. Phys.* 229 (2010), 9092-9118.
- [23] R. Li, T. Tang, and P. W. Zhang, Moving mesh methods in multiple dimensions based on harmonic maps. *J. Comput. Phys.* 170 (2001), 562-588.
- [24] H. Luo, J. D. Baum, and R. Löhner, On the computation of multi-material flows using ALE formulation, *J. Comput. Phys.* 194 (2004), 304-328.
- [25] P.-H. Maire, R. Abgrall, J. Breil, R. Loubère, and B. Rebourecet, A nominally second-order cell-centered Lagrangian scheme for simulating elastic-plastic flows on two-dimensional unstructured grids. *J. Comput. Phys.* 235 (2013), 626-665.

- [26] I. Menshov, A. Mischenko, and A. Serezhkin, An Eulerian Godunov-type scheme for calculation of the elastic-plastic flow equations with moving grids. In: 6th European Congress on Computational Methods in Applied Sciences and Engineering 2012 (ECCOMAS 2012), Vienna, Austria, September 10-14, 2012, pp. 4099-4118.
- [27] K. Miller and R. N. Miller, Moving finite elements I. *SIAM J. Numer. Anal.* 18 (1981), 1019-1032.
- [28] G. H. Miller and P. Collela, A high-order Eulerian Godunov method for elastic-plastic flow in solids. *J. Comput. Phys.* 167 (2001), 131-176.
- [29] V. T. Nguyen, An arbitrary Lagrangian-Eulerian discontinuous Galerkin method for simulations of flows over variable geometries, *J. Fluid Struct.* 26 (2010), 312-329.
- [30] A. K. Pandare, C. Wang, and H. Luo, An arbitrary Lagrangian-Eulerian reconstructed Discontinuous Galerkin method for compressible multiphase flows, 46th AIAA fluid dynamic conference, June 2016, DOI:10.2514/6.2016-4270.
- [31] S. K. Sambasivan, R. Loubere and M. J. Shashkov, A finite volume Lagrangian cell-centered mimetic approach for computing elastoplastic deformation of solids in general unstructured grids, In: 6th European Congress on Computational Methods in Applied Sciences and Engineering 2012 (ECCOMAS 2012), Vienna, Austria, September 10-14, 2012.
- [32] T. Tang. Moving mesh methods for computational fluid dynamics flow and transport. In *Recent Advances in Adaptive Computation (Hangzhou, 2004)*, volume 383 of *AMS Contemporary Mathematics*, pages 141–173. Amer. Math. Soc., Providence, RI, 2005.
- [33] E. F. Toro. Riemann Solvers and Numerical Methods for Fluid Dynamics, Springer Dordrecht Heidelberg London New York, 1997.
- [34] J. A. Trangenstein and P. Collela, A high-order Godunov method for modeling finite deformation in elastic-plastic solids. *Comm. Pure Appl. Math.* XLIV (1991), 41-100.
- [35] M. L. Wilkins, Methods in Computational Physics, Vol.3, Chapter Calculation of elastic-plastic flow, Academic Press, 1964, pp. 211-263.